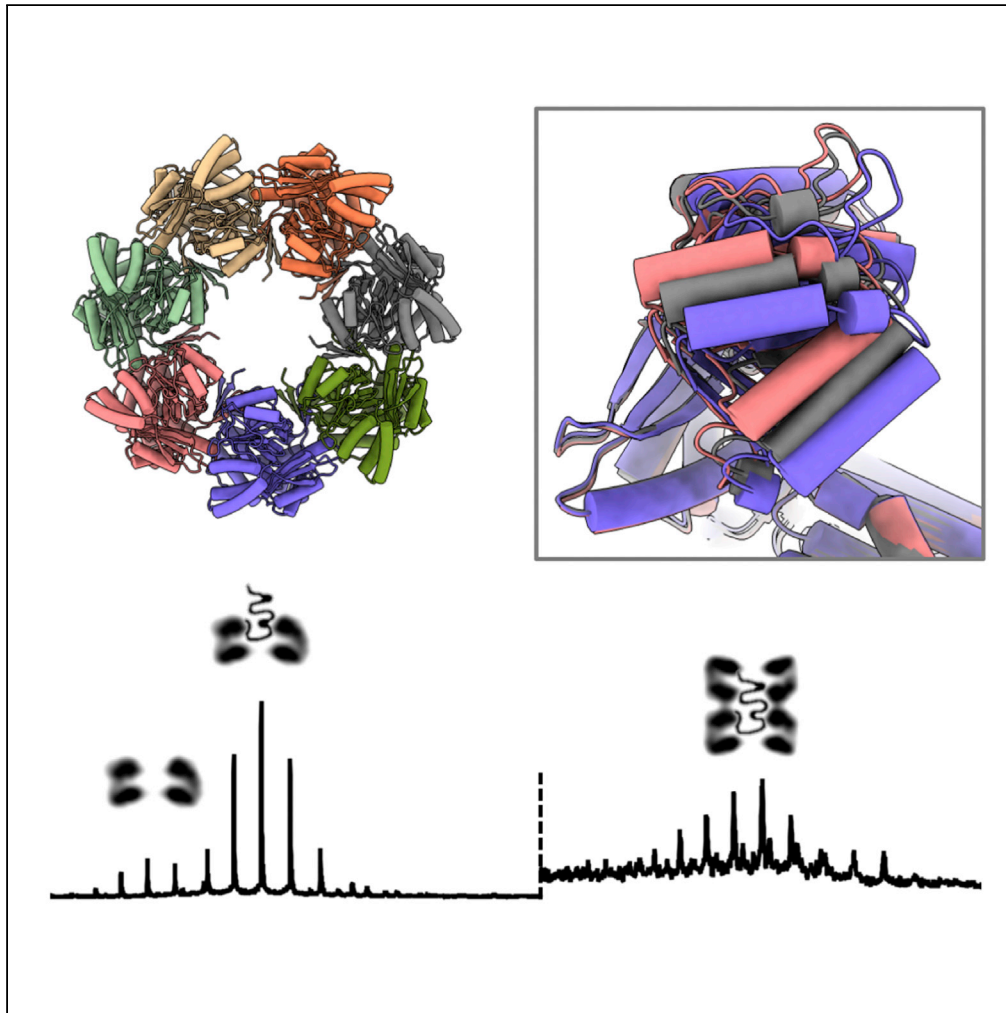


Article

Cryo-EM structure of human mitochondrial HSPD1



David P. Klebl,
Matthew C.
Feasey, Emma L.
Hesketh, ..., Frank
Sobott, Robin S.
Bon, Stephen P.
Muench

s.p.muench@leeds.ac.uk

HIGHLIGHTS

First cryo-EM structure of
the apo HSPD1 chaperone
complex

Mass spectrometry has
shown the presence of 7,
8, 15, and 16-mers of
HSPD-1

In addition to a single ring,
HSPD-1 can form an
unusual inverted ring
architecture

Describe grid preparation
conditions that alleviate
preferred orientation

Klebl et al., iScience 24,
102022
January 22, 2021 © 2020
[https://doi.org/10.1016/
j.isci.2020.102022](https://doi.org/10.1016/j.isci.2020.102022)

Article

Cryo-EM structure of human mitochondrial HSPD1

David P. Klebl,¹ Matthew C. Feasey,¹ Emma L. Hesketh,² Neil A. Ranson,² Heiko Wurdak,³ Frank Sobott,^{2,4} Robin S. Bon,⁵ and Stephen P. Muench^{1,6,*}

SUMMARY

Chaperonins play an important role in folding newly synthesized or translocated proteins in all organisms. The bacterial chaperonin GroEL has served as a model system for the understanding of these proteins. In comparison, its human homolog, known as mitochondrial heat shock protein family member D1 (HSPD1) is poorly understood. Here, we present the structure of HSPD1 in the apo state determined by cryo-electron microscopy (cryo-EM). Unlike GroEL, HSPD1 forms mostly single ring assemblies in the absence of co-chaperonin (HSPE1). Comparison with GroEL shows a rotation and increased flexibility of the apical domain. Together with published structures of the HSPD1/HSPE1 co-chaperonin complex, this work gives insight into the structural changes that occur during the catalytic cycle. This new understanding of HSPD1 structure and its rearrangements upon complex formation may provide new insights for the development of HSPD1-targeting treatments against a diverse range of diseases including glioblastoma.

INTRODUCTION

Chaperonins are molecular chaperones forming ring-shaped complexes that catalyze protein folding through the capture of unfolded polypeptides and confinement within a central cavity driven by ATP hydrolysis (Horwich et al., 2007). Bacterial GroEL, a type I chaperonin, has served as a model system to understand the structural characteristics and mechanism of chaperonins (Levy-Rimler et al., 2002). GroEL is essential in bacteria and involved in folding about 10%–15% of newly synthesized proteins (Hartl and Hayer-Hartl, 2002). The GroEL complex has been extensively studied using structural and biochemical methods over the last decades, leading to a good mechanistic understanding of its structure and function (Horwich and Fenton, 2020). GroEL forms a homo-tetradecameric structure, in which two heptameric rings are stacked back to back (Braig et al., 1994). During its catalytic cycle, GroEL binds substrate protein, ATP, and co-chaperonin GroES to form a nanoreactor in which substrate proteins can fold. Upon ATP hydrolysis, GroES, nucleotides, and substrate proteins are released (Bukau and Horwich, 1998). ATP and GroES binding between the two rings is coupled by negative cooperativity, whereas ATP binding within one ring is positively cooperative (Saibil et al., 2013; Dyachenko et al., 2013). This cooperativity is thought to be important for function: a mutant GroEL, forming single rings and lacking the negative inter-ring cooperativity, gives rise to dead-end complexes (Weissman et al., 1995).

The human homolog of GroEL is mitochondrial HSPD1, which is essential and responsible for (re)-folding of nuclear-encoded proteins that are imported into the mitochondria as well as polypeptides encoded by mtDNA (Kampinga et al., 2009). Aberrant substrate folding can lead to a variety of neurodegenerative disorders including Alzheimer, Parkinson, and Creutzfeldt-Jacob disease (Sato et al., 2005; Chiti and Dobson 2006) that may correlate with an age-dependent decline in protein quality control (van der Putten and Lotz 2013). Mutations in HSPD1 have been associated with the hereditary brain diseases spastic paraplegia (Hansen et al. 2002, 2007) and autosomal-recessive neurodegenerative disorder (Magen et al., 2008). In the aggressive brain cancer glioblastoma, elevated HSPD1 expression confers poor prognosis and is linked with mitochondrial energy metabolism (Polson et al., 2018). Moreover, HSPD1 has been implicated in cancer proliferation and apoptosis (Cappello et al., 2014) as well as inflammatory and autoreactive conditions (Pockley et al., 2014).

Compared with GroEL, less structural and biochemical insight exists for HSPD1 (Levy-Rimler et al., 2002). Complexes of HSPD1 are unstable *in vitro* and dissociate in a time- and temperature-dependent manner (Viitanen et al., 1998). Upon reconstitution, HSPD1 forms mainly single ring assemblies instead of double rings (Viitanen et al., 1992). In complex with the co-chaperonin HSPE1 (the human GroES homolog),

¹School of Biomedical Sciences, Faculty of Biological Sciences & Astbury Centre for Structural and Molecular Biology, University of Leeds, Leeds LS2 9JT, UK

²School of Molecular and Cellular Biology, Faculty of Biological Sciences & Astbury Centre for Structural and Molecular Biology, University of Leeds, Leeds LS2 9JT, UK

³School of Medicine, Faculty of Medicine and Health, Stem Cell and Brain Tumour Group, University of Leeds, Leeds LS9 7TF, UK

⁴Department of Chemistry, Biomolecular & Analytical Mass Spectrometry Group, University of Antwerp, Antwerp, Belgium

⁵School of Medicine, Faculty of Medicine and Health & Astbury Centre for Structural and Molecular Biology, University of Leeds, LS2 9JT Leeds, UK

⁶Lead contact

*Correspondence: s.p.muench@leeds.ac.uk
<https://doi.org/10.1016/j.isci.2020.102022>



HSPD1 single and double ring assemblies have been shown to coexist. Specifically, there is evidence for single ring HSPD1₇/HSPE1₇ (half-football) and double ring HSPD1₁₄/HSPE1₁₄ (football) complexes; however, the precise order in the catalytic cycle has not been elucidated (Levy-Rimler et al., 2001). In contrast to GroEL, HSPD1 shows less requirement for inter-ring cooperativity, and HSPD1 mutants with impaired double ring formation can remain fully functional. The recently published structures of the ADP-BeF₃-bound football complex and the ADP-bound football and half-football complexes represent a large step toward understanding the differences and similarities between GroEL- and HSPD1-catalyzed protein folding (Gomez-Llorente et al., 2020). Increasing evidence indicates distinct structure and enzymatic mechanism of bacterial and human chaperonins; however, an atomic model of apo HSPD1 has not been reported to date.

A potential reason for the lack of a high-resolution apo HSPD1 structure is the instability of its reconstituted oligomers. Although compositional heterogeneity can be accounted for by particle classification in cryo-electron microscopy (cryo-EM), our previous efforts to obtain a high-resolution structure were complicated by strong preferred particle orientation on cryo-EM grids. In this work, by optimization of particle concentration and buffer conditions, the structure of apo HSPD1 single ring was determined at 3.5 Å. The structure shows high similarity to GroEL and reveals high flexibility of the apical domains. Side-by-side comparison with a HSPD1/E1 complex structure shows conformational changes during the catalytic cycle. We also show that two apo HSPD1 single rings can dimerize in an unusual manner, forming an inverted double ring. The structure of apo HSPD1 represents a further important step in understanding the conformational landscape of the HSPD1 chaperonin.

RESULTS

Reconstitution of HSPD1 into oligomers

For the structural studies, HSPD1 was expressed without the mitochondrial target peptide. Overexpression of mature human mitochondrial HSPD1 in *Escherichia coli* resulted in a high yield of protein (amount: ~ 30 mg per 1 L of culture), purified in monomeric form. The HSPD1 oligomer was then reconstituted in the presence of ATP followed by size exclusion chromatographic purification (Figures 1A and 1B). Characterization of the oligomeric fraction by negative stain EM revealed the characteristic 7-fold symmetrical shape for chaperonins as previously described for the HSPD1 single ring (Figure 1C).

Stoichiometry of the reconstituted HSPD1 complex was analyzed by native mass spectrometry (MS) (Figure 1D). Masses for the main oligomeric species (Figure 1D) were 407,635 ± 90 Da and 465,849 ± 82 Da, corresponding to assemblies of 7 and 8 subunits, respectively. Although the heptameric assembly was expected based on the negative stain EM results and previous work (Viitanen et al., 1992), the detection of 8-mer shows that an additional subunit can bind the heptameric form. The mass accuracy is sufficient to determine that, on average, the nucleotide binding site was free. In addition, the mass spectra showed species corresponding to 1, 2, 15, and 16 subunits, which are further discussed later.

Cryo-EM of oligomeric apo HSPD1

Initial attempts to determine the structure of HSPD1 by cryo-EM resulted in reconstructions at medium resolutions (5–10 Å). The major component identified by cryo-EM was the single toroidal ring with clear 7-fold symmetry. Well-distributed particles were present in the ice, and the picked particles produced well-resolved 2D classes showing distinct secondary structure. However, the resultant 3D reconstruction was significantly hindered by preferred orientation showing almost exclusively the 7-fold symmetrical top views. To alleviate problems of preferred orientation, we screened a range of conditions including carbon or graphene oxide support grids and amylamine glow discharge, none of which gave any clear improvements in angular distribution.

We used novel fast grid preparation techniques as an alternative, with a home-built device designed for time-resolved EM or a chameleon grid-making device (SPT Labtech). This could not eliminate binding to the air-water interface but gave modest improvements in angular distribution, but, in the case of the home-built device, it also increased ice thickness (Klebl et al., 2020).

Grids prepared by conventional blotting at ambient temperature (when compared with the 5°C–6°C routinely used for plunge freezing) required much higher sample concentrations to achieve the same protein density on the grids (≥ 1 mg/mL at 20°C versus 0.25 mg/mL at 5°C). This was counterintuitive as HSPD1 oligomers have been shown to be less stable at low temperatures (Viitanen et al., 1998). Preparing grids at

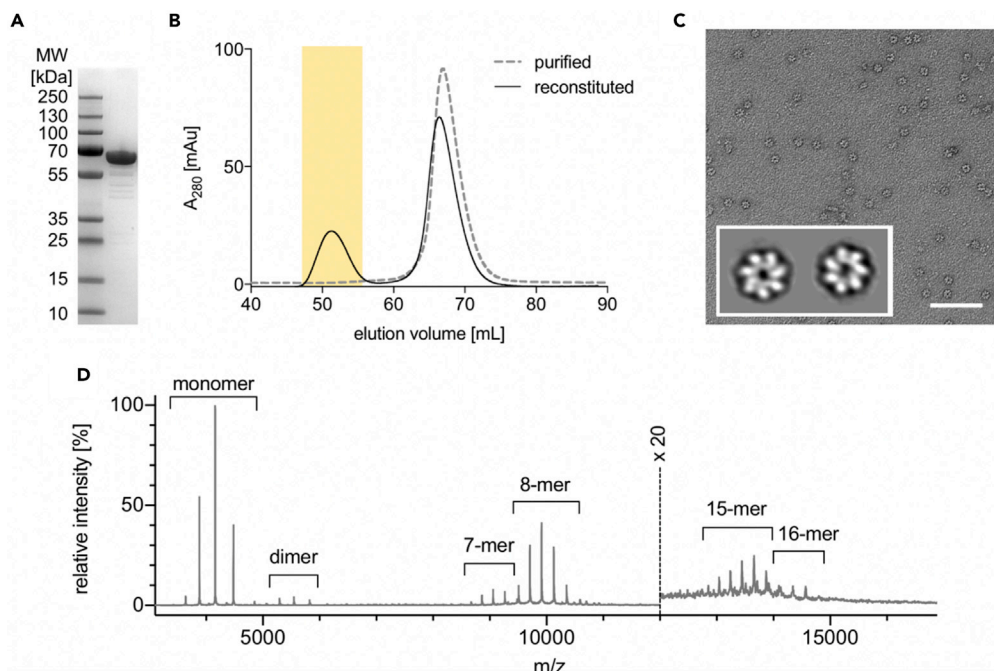


Figure 1. Reconstitution and characterization of HSPD1 oligomers

(A) SDS PAGE gel for purified HSPD1 monomer.

(B) Size exclusion chromatography of purified (gray dashed line) and reconstituted (black solid line) HSPD1 with the peak for oligomeric HSPD1 highlighted in yellow.

(C) Negative stain electron micrograph of the oligomeric HSPD1 (scale bar, 100 nm). The inset shows two representative 2D classes.

(D) Native mass spectrum of reconstituted HSPD1 showing multiple charge state distributions; different species are labeled. Above 12,000 m/z, the spectral intensity has been multiplied by 20.

~20°C and high protein concentration (2.3 mg/mL) resulted in a small increase in angular spread, presumably due to significant crowding at the air-water interface. Yet, this approach still yielded anisotropic reconstructions, and the overall resolution was limited to ~4 Å. Using an optimized buffer, which included 1 mM DTT for grid preparation, high concentration and conventional blotting yielded the final reconstruction at a global resolution of 3.5 Å (Figure 2) with C7 symmetry. The reconstruction showed no significant anisotropy, and the resolution was sufficient to enable atomic modeling based on previous apo-GroEL and the HSPD1-HSPE1 complex crystal structures (Figure 2 and Table 1).

The seven resolved subunits show the typical three-domain chaperonin structure (Figure 2C). The equatorial domain forms the well-resolved base of the single ring (residues 1–134, 409–524), mainly composed of α -helices. The apical domain (residues 189–372) at the top of the ring contains two β -sheets and five α -helices. Among these are helices H and I (residues 232–240 and 254–266, respectively), lining the top of the central cavity. Last, the intermediate (hinge) domain (residues 135–188, 373–408) connects the equatorial and apical domains.

Conformational variability of HSPD1 subunits within the complex

Apart from the differences in complex stoichiometry (single ring) the structures of apo HSPD1 and GroEL (PDB: 1xck, Bartolucci et al., 2005) are highly similar on the subunit level, as expected with 51% sequence identity. The highest structural similarity is found around the equatorial domain, which is the most rigid and therefore best resolved region in the HSPD1 cryo-EM map. The most apparent difference in structure is an increased deviation between the apical domains (~2.6 Å average root-mean-square deviation) of HSPD1 and GroEL.

The lower local resolution in the region of the apical domain led us to examine conformational variability in the apical domain in more detail. This was done by symmetry expansion and focused classification into 10 classes (Figure S3). Only classes with clear density for helices H and I (the polypeptide binding site on the

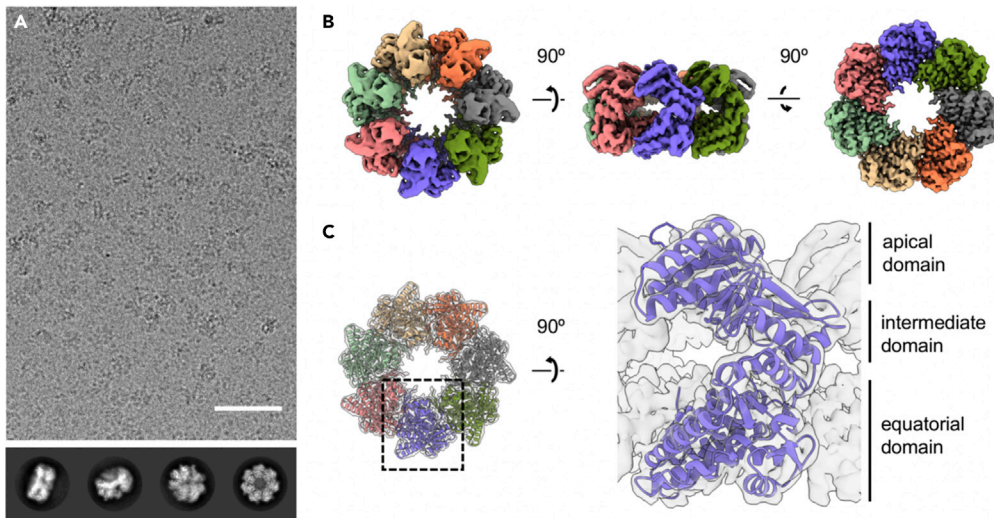


Figure 2. Cryo-EM structure of HSPD1 single ring

(A) Raw micrograph of apo HSPD1 (scale bar, 50 nm). The bottom panel shows representative 2D classes from the final particle selection.

(B) Cryo-EM reconstruction of the apo HSPD1 single ring at 3.5 Å, colored by subunit.

(C) Atomic model for apo HSPD1 in the EM density (transparent). On the right, one subunit is shown from the side, and the three domains are labeled.

apical domain) were taken forward. These eight classes show variable positioning of helices H and I relative to the equatorial domain (Figure 3A). Atomic models for each class were generated by flexible fitting and show that the range of conformations within the data is large (Figure 3B). The distance between equatorial domain residue Trp42 and Asn239, for example, varies more than 5 Å between classes 3 and 10. Plotting the distance Trp42-Asn239 (equatorial/helix H) against the distance Trp42-Gly254 (equatorial/helix I) shows how the different conformations fall into clusters (Figure 3C). Class 3 resembles the most compact form in which apical and equatorial are closest. Most subunits adopt a conformation similar to class 8 (the central region in Figure 3C). Classes 4 and 10 represent a third class of conformation, which is more “extended” with the largest distances between apical and equatorial domains. Generally, the points in Figure 3C lie along the diagonal, which would be expected for a concerted movement of the apical domain.

Class 3 is most similar to GroEL regarding the apical domain position, whereas in the more predominant conformers (65% of subunits) the apical domain is rotated upward. This shows that HSPD1 subunits can adopt a range of conformations, some of which are very similar to GroEL, but that more extended forms of HSPD1 are preferred.

Comparison of apo HSPD1 with the half-football complex structure of HSPD1 and HSPE1

For comparison to the HSPD1/HSPE1 co-complex, we chose the ADP-bound half-football HSPD1₇/HSPE1₇ (PDB: 6mrd, Gomez-Llorente et al., 2020) as a reference as it should represent the nearest neighbor in the catalytic cycle. Relative to the half-football, the apical domains of apo HSPD1 undergo a large rigid body motion, resulting in an overall ~66° rotation (Figure 4A), which is comparable to structural changes in GroEL between ADP/GroES-bound and -unbound states and required to allow HSPE1 binding in the half-football state.

Smaller differences can be found in the equatorial domain, located mostly around the nucleotide binding site. For instance, the short loop containing Asp85, which is involved in Mg-ADP coordination in the half-football structure, is located further toward the nucleotide binding site in the apo state (Figure 4B).

The position of two strands involved in forming the inter-subunit β-sheet (residues 36–38 and 46–48) is altered in apo HSPD1 relative to the half-football complex (Figure 4C). To understand the significance of this change in inter-subunit contacts, the entire single rings (HSPD1 and half-football) were aligned on their equatorial domains. This revealed a rotation of 17° for the HSPD1 equatorial domain relative to the half-football, whereas the radial distance from the ring center remained virtually unchanged (Figure 4D).

Table 1. Summary of data collection/processing parameters and model building statistics. FSC stands for Fourier Shell Correlation.

Data collection and processing	HSPD1 single ring
Magnification	×75,000
Voltage (kV)	300
Electron exposure (e ⁻ /Å ²)	38.5
Defocus range (μm)	1.5 to 3
Pixel size (Å)	1.065
Symmetry imposed	C7
Initial particle images (no.)	355,766
Final particle images (no.)	124,784
Map resolution (Å)	3.5
FSC threshold	0.143
Map resolution range (Å)	3.2–4.8
Refinement	
Initial models used	PDB: 4pj1, 1xck
Map resolution (Å)	3.4
FSC threshold	0.5
Map sharpening B factor (Å ²)	–100
Model composition	
Non-hydrogen atoms	27,391
Protein residues	3,675
B factors (Å²)	
Protein	123
Root mean square deviations	
Bond lengths (Å)	0.004
Bond angles (°)	0.611
Validation	
MolProbity score	1.74
Clashscore	10.53
Poor rotamers (%)	0.71
Ramachandran plot	
Favored (%)	96.75
Allowed (%)	3.25
Disallowed (%)	0

FSC stands for Fourier Shell Correlation.

Different oligomeric states of the HSPD1 complex

Native MS showed the presence of multiple oligomeric species in the reconstituted sample (Figure 1D). The masses obtained from the six main charge state distributions are given in Table 2. They were assigned to monomer, dimeric, heptameric, octameric, 15-meric, and 16-meric assemblies, with a theoretical monomer mass of 58,235.12 Da.

The monomeric and dimeric species are most likely dissociation products from larger oligomers, due to the instability of HSPD1 complexes. Heptameric and octameric species were assigned to the single ring, with or without an additional subunit bound. The larger assemblies, 15-mer and 16-mer, probably correspond to higher-order complexes composed of two single rings.

In agreement with the MS analysis, cryo-EM data under certain buffer conditions (50 mM Tris, 300 mM NaCl, 10 mM MgCl₂) contained a small fraction of double ring particles (up to 8.3%, Figures 5A and 5B). We note

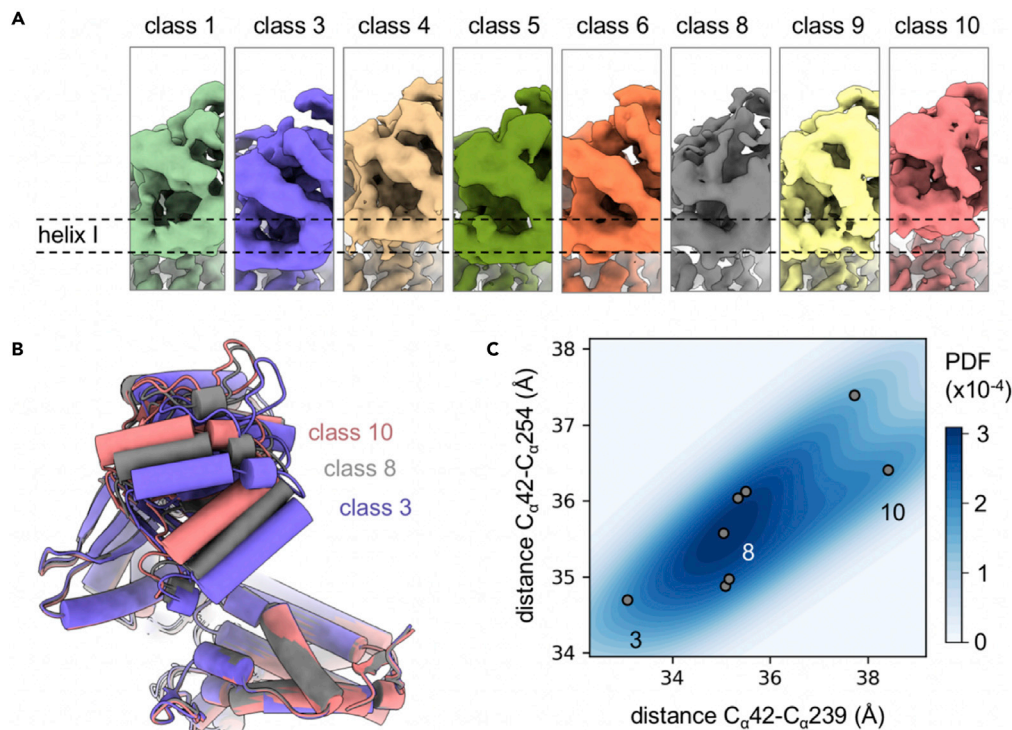


Figure 3. Conformational variability in the apical domain

(A) Eight subunit reconstructions show variable apical domain positions. The position of helix I in class 1 is indicated by dotted lines to help compare the classes.

(B) Overlay of flexibly fitted models for classes 3, 8, and 10 in purple, gray, and light red.

(C) Plot of measured equatorial/apical domain distances for all eight classes. Each class is represented by a gray point; classes 3, 8 and 10 are labeled. Points approximately lie on the diagonal, showing that the entire apical domain rotates upward. The background color is an estimate of the probability to find a subunit in a certain conformation, taking the particle number in each class into account. PDF stands for probability density function.

that the relative amount of those particles varied, depending on the grid preparation and buffer conditions. Processing of the double ring species resulted in a 4.9 Å reconstruction with D7 symmetry. At this resolution the densities for the seven individual subunits per ring did not show any significant structural differences from the single ring. Unexpectedly, the overall structure is an inverted double ring, in which the two single rings contact each other face to face, with their apical domains. This arrangement is also apparent from the 2D class averages, and there was no occurrence of a different arrangement, confirming the face-to-face arrangement is either the sole or dominant species. The dimerization interface shows remarkably few interactions between the two single rings, with potential interacting residues His241, Gln312, Pro313, and His314 (Figure 5C).

DISCUSSION

HSPD1 oligomers were prepared using established methods and the structure solved by single particle cryo-EM. Native MS revealed complexes with seven and eight subunits as the major oligomeric species. We propose that both heptameric and octameric HSPD1 adopt the single ring architecture observed in cryo-EM. The octameric complex must contain one additional subunit, but we see no evidence for an 8-fold symmetric complex in 2D classification suggesting that the additional subunit is disordered and bound as a substrate. HSPD1 can self-chaperone *in vitro* and *in vivo*, and the purified complex has limited stability, which explains the presence of monomers in sample (Cheng et al., 1990). Binding of these monomers by the remaining intact single rings is a plausible mechanism for formation of octameric complex (Figure 5D). This observation is consistent with previous multi-angle laser scattering measurements of apo HSPD1 oligomers, giving mass estimates of ~450 kDa, which could be explained by a mixture of heptameric and octameric complex (Levy-Rimler et al., 2001; Gomez-Llorente et al., 2020).

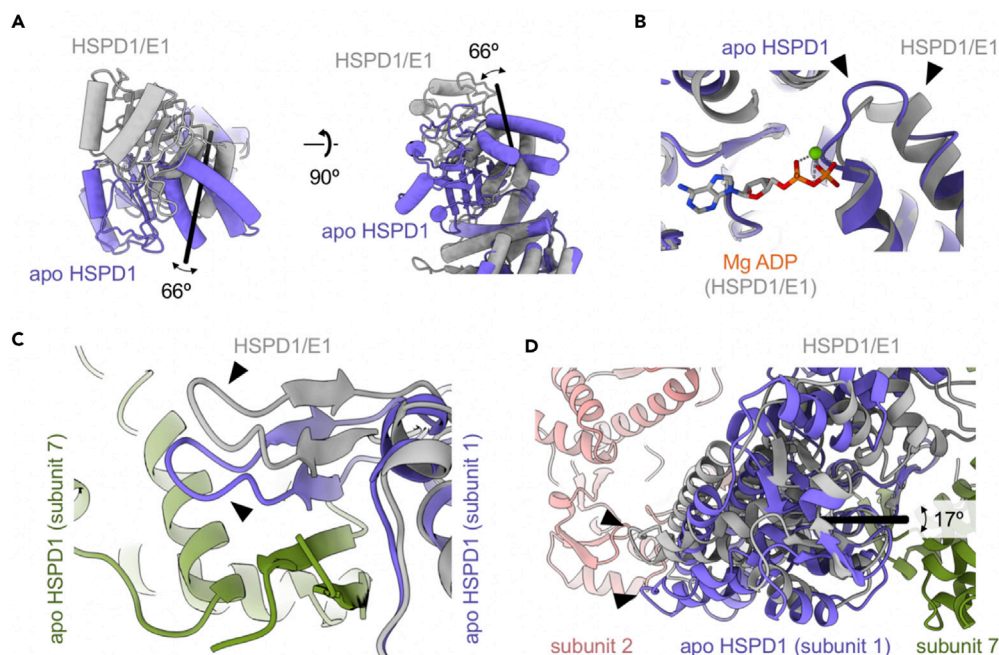


Figure 4. Comparing structures of apo HSPD1 and the half-football complex (HSPD1₇/HSPE1/MgADP)

In all panels, the half-football complex is shown in gray (orange and green for neighboring subunits), and the corresponding apo HSPD1 subunit is shown in purple. Arrowheads are used to indicate the regions that show the biggest change.

- (A) Rotation of the apical domain. Shown are the top (left) and side views of the domain (right). The black line is the rotation axis.
 (B) Small changes near the nucleotide binding site involving Asp85.
 (C) Altered position of the inter-subunit beta sheet in apo HSPD1 between subunits 1 and 7.
 (D) Relative rotation of the equatorial domains in the single ring. The rotation axis is shown as black line.

Compared with GroEL or double ring structures of the HSPD1/E1 complex, the inverted double ring of HSPD1 requires each ring to be rotated by 180° perpendicular to their 7-fold symmetry axes (Figure 5D). This mode of ring dimerization also occludes the HSPE1 binding site on the apical domain. In the inverted double ring structure, the apical domains containing the polypeptide binding sites are facing each other. We hypothesize that the additional one or two subunits in the double ring (14 subunits resolved by cryo-EM and 15 or 16 by native MS) are placed in the center of the complex (Figure 5D). Binding of one or two disordered subunits by two single rings would also strengthen the apparently weak interface between the two rings. The face-to-face double ring arrangement has not been described for group I chaperonins, but a similar interface has recently been reported for a group II archaeal chaperonin, proposed to be a resting state (Zeng et al., 2020). Although our data show the presence of the inverted double ring *in vitro*, its relevance *in vivo* remains unclear.

The predominant form of apo HSPD1, the single ring, was compared with apo GroEL revealing an overall difference in the position of the apical domain. In GroEL, salt bridges Arg197/Glu386 and Lys207/Glu255 between neighboring apical domains and the equatorial/apical salt bridge Asp83/Lys327 are thought to stabilize the position of the apical domain (Horwich and Fenton, 2020). Interestingly, GroEL Lys207 aligns with Thr205 in the HSPD1 sequence. In HSPD1, there is a Lys two positions downstream in the sequence, which occupies a similar position to GroEL Lys207 and may cause the upward movement of the apical domain. The presence of 27% subunits without clear density for helices H or I suggests that the true number of conformations could be larger with greater motion, than what has been captured by the analysis in this work. Conformational flexibility has also been observed in GroEL, although to a lesser extent, and is thought to be important for substrate promiscuity (Roh et al., 2017; Chen and Sigler, 1999). This conformational variability is likely limiting local resolution in the apical domain and possibly also global resolution.

A structural comparison with the nearest available neighbor in the HSPD1 catalytic cycle, namely, the ADP-bound half-football, provided insight into the conformational changes upon HSPE1/ADP release. The

Table 2. Table of observed and calculated masses for oligomeric species by native mass spectrometry

Observed mass (Da)	Experimental error (Da)	Main charge state	Number of subunits	Theoretical mass (Da)
58,235	15	14+	1	58,235
116,470	32	21+	2	116,470
407,635	90	45+	7	407,646
465,849	82	47+	8	465,881
873,978	480	64+	15	873,527
932,402	640	64+	16	931,762

rearrangements between apo HSPD1 and the HSPD1/E1 half-football resemble the corresponding conformational states in GroEL closely. This suggests a similar allosteric network throughout the molecule. The complete lack of inter-ring cooperativity during the catalytic cycle of HSPD1 therefore seems surprising (Gomez-Llorente et al., 2020).

The present work provides new insights into HSPD1 complex composition and conformation, but further research is needed to understand conformational changes in HSPD1 and the order of states in the catalytic cycle. This will be essential for pharmacological targeting of the chaperonin system in HSPD1-mediated disease. For example, insight into the HSPD1 apical domain movement required for complex formation with HSPE1 may provide new opportunities for the development of inhibitors of this protein-protein interaction (PPI), a major challenge because of the relatively low affinity of the PPI (K_D 7.0 μ M) and the large buried surface area involved ($\sim 5,500$ \AA^2) (Gestwicki and Shao, 2019).

This work provides the first atomic model of the HSPD1 chaperone in the apo state. It highlights the common mechanisms conserved between the well-characterized bacterial system and the less understood human mitochondrial homolog. Although significant strides in our understanding of chaperones have been achieved through studies of the bacterial GroEL complex, this work provides new insights into the human HSPD1 chaperone and highlights that direct study of this system is key if we are to design specific modulators of function that can provide potent new therapeutics.

Limitations of the study

This work provides the first structure of the HSPD1 complex, but many questions remain unanswered. We do not know the physiological significance of the double ring that is seen in both EM and MS experiments. Although a similar interaction has been seen for a group II archaeal chaperonin (Zeng et al., 2020), only time will tell if this interaction is physiologically relevant. We provide evidence for an 8-mer where we predict that one HSPD1 subunit is acting as a substrate for the 7-mer. This additional subunit appears to be highly dynamic and disordered, and therefore we could not resolve it by cryo-EM.

Protein folding requires a multipart mechanical cycle with HSPD1 forming a complex with HSPE in either a half-football (HSPD1₇/HSPE1₇) or football (HSPD1₁₄/HSPE1₁₄). Further work will be required to determine the precise order in the catalytic cycle with techniques such as time-resolved cryo-EM.

Resource availability

Lead contact

Further requests for resources and reagents should be directed to and will be fulfilled by the Lead Contact, Stephen Muench (s.p.muench@leeds.ac.uk).

Materials availability

No new reagents were generated in this study.

Data and code availability

The atomic model and map for the HSPD1 single ring have been deposited to the PDB and EMDB with accession codes PDB: 7AZP and EMD: 11950, respectively. A map for the inverted double ring has been deposited to the EMDB with accession code EMD: 11189.

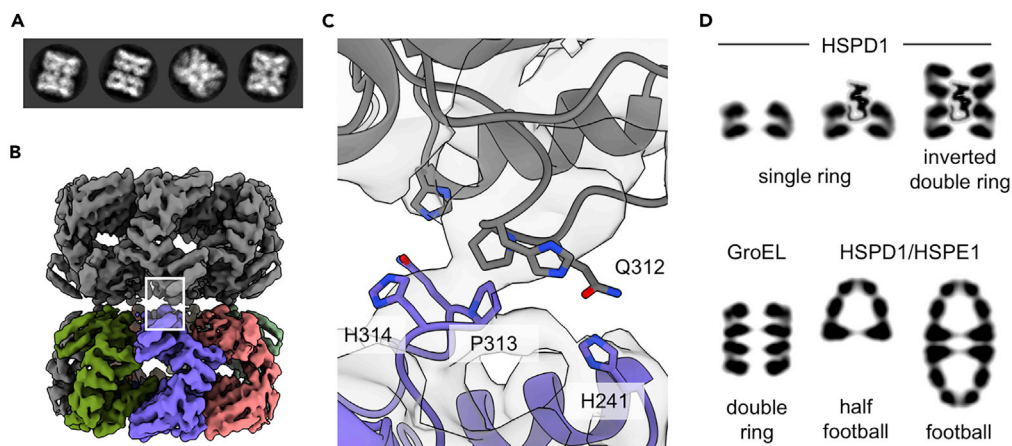


Figure 5. The HSPD1 inverted double ring

(A) Selected 2D classes of the inverted double ring.

(B) D7-symmetrical reconstruction of the inverted double ring with one ring colored by subunit and the second ring in gray. The interface between the two rings is highlighted by the white rectangle.

(C) Magnified view of the inter-ring interface of the double ring with potential interacting residues labeled.

(D) Schematic of the HSPD1 oligomeric states, apo GroEL, and HSPD1/HSPE1 complexes in comparison. Depicted are central sections of side views for the complexes. The eighth subunit is not resolved by cryo-EM, thus probably disordered, and has been placed in the substrate binding site on the apical domains. According to native MS data, the inverted double ring may contain one or two additional (unresolved) subunits.

METHODS

All methods can be found in the accompanying [Transparent methods supplemental file](#).

SUPPLEMENTAL INFORMATION

Supplemental Information can be found online at <https://doi.org/10.1016/j.isci.2020.102022>.

ACKNOWLEDGMENTS

The authors would like to thank Dr. Hao Shao and Dr. Jason Gestwicki (UCSF) for providing the HSPD1 plasmid. D.P.K. is a PhD student on the Wellcome Trust 4-year PhD program in The Astbury Center funded by The University of Leeds. The Titan Krios microscopes were funded by the University of Leeds (UoL ABSL award) and Wellcome Trust (108466/Z/15/Z). The time-resolved device was developed by a Biotechnology and Biological Sciences Research Council grant BB/P026397/1. The Orbitrap UHMR was funded by Wellcome Trust multi-user equipment grant 208385/Z/17/Z.

AUTHOR CONTRIBUTIONS

Conceptualization and experimental design, D.P.K., M.C.F., E.L.H., N.A.R., H.W., F.S., R.S.B., and S.P.M.; performed experiments, D.P.K., M.C.F., and E.L.H.; analysis of data: D.P.K., M.C.F., E.L.H., N.A.R., F.S., R.S.B., and S.P.M.; Supervision, N.A.R., F.S., R.S.B., and S.P.M.; wrote the manuscript, D.P.K., M.C.F., H.W., F.S., R.S.B., and S.P.M.

DECLARATION OF INTERESTS

The authors declare no conflicts of interest.

Received: September 1, 2020

Revised: November 17, 2020

Accepted: December 29, 2020

Published: January 22, 2021

REFERENCES

- Bartolucci, C., Lamba, D., Grazulis, S., Manakova, E., and Heumann, H. (2005). Crystal structure of wild-type chaperonin GroEL. *J. Mol. Biol.* 354, 940–951.
- Braig, K., Otwinowski, Z., Hegde, R., Boisvert, D.C., Joachimiak, A., Horwich, A.L., and Sigler, P.B. (1994). The crystal structure of the bacterial chaperonin GroEL at 2.8 Å. *Nature* 371, 578–586.
- Bukau, B., and Horwich, A.L. (1998). The Hsp70 and Hsp60 chaperone machines. *Cell* 92, 351–366.
- Cappello, F., Marino Gammazza, A., Palumbo Piccionello, A., Campanella, C., Pace, A., Conway de Macario, E., and Macario, A.J. (2014). Hsp60 chaperonopathies and chaperonotherapy: targets and agents. *Expert Opin. Ther. Targets* 18, 185–208.
- Chen, L., and Sigler, P.B. (1999). The crystal structure of a GroEL/peptide complex: plasticity as a basis for substrate diversity. *Cell* 99, 757–768.
- Cheng, M.Y., Hartl, F.U., and Horwich, A.L. (1990). The mitochondrial chaperonin hsp60 is required for its own assembly. *Nature* 348, 455–458.
- Chiti, F., and Dobson, C.M. (2006). Protein misfolding, functional amyloid, and human disease. *Annu. Rev. Biochem.* 75, 333–366.
- Dyachenko, A., Gruber, R., Shimon, L., Horovitz, A., and Sharon, M. (2013). Allosteric mechanisms can be distinguished using structural mass spectrometry. *Proc. Natl. Acad. Sci. USA* 110, 7235–7239.
- Gestwicki, J.E., and Shao, H. (2019). Inhibitors and chemical probes for molecular chaperone networks. *J. Biol. Chem.* 294, 2151–2161.
- Gomez-Llorente, Y., Jebara, F., Patra, M., Malik, R., Nisemblat, S., Chomsky-Hecht, O., Parnas, A., Azem, A., Hirsch, J.A., and Ubarretxena-Belandia, I. (2020). Structural basis for active single and double ring complexes in human mitochondrial Hsp60-Hsp10 chaperonin. *Nat. Commun.* 11, 1916–2014.
- Hansen, J.J., Dürr, A., Cournu-Rebeix, I., Georgopoulos, C., Ang, D., Nielsen, M.N., Davoine, C.S., Brice, A., Fontaine, B., Gregersen, N., and Bross, P. (2002). Hereditary spastic paraplegia SPG13 is associated with a mutation in the gene encoding the mitochondrial chaperonin Hsp60. *Am. J. Hum. Genet.* 70, 1328–1332.
- Hansen, J., Svenstrup, K., Ang, D., Nielsen, M.N., Christensen, J.H., Gregersen, N., Nielsen, J.E., Georgopoulos, C., and Bross, P. (2007). A novel mutation in the HSPD1 gene in a patient with hereditary spastic paraplegia. *J. Neurol.* 254, 897.
- Hartl, F.U., and Hayer-Hartl, M. (2002). Molecular chaperones in the cytosol: from nascent chain to folded protein. *Science* 295, 1852–1858.
- Horwich, A.L., and Fenton, W.A. (2020). Chaperonin-assisted protein folding: a chronologue. *Q. Rev. Biophys.* 53, e4.
- Horwich, A.L., Fenton, W.A., Chapman, E., and Farr, G.W. (2007). Two families of chaperonin: physiology and mechanism. *Annu. Rev. Cell Dev. Biol.* 23, 115–145.
- Kampinga, H.H., Hageman, J., Vos, M.J., Kubota, H., Tanguay, R.M., Bruford, E.A., Cheetham, M.E., Chen, B., and Hightower, L.E. (2009). Guidelines for the nomenclature of the human heat shock proteins. *Cell Stress Chaperones* 14, 105–111.
- Klebl, D.P., Gravett, M.S., Kontziampasis, D., Wright, D.J., Bon, R.S., Monteiro, D., Trebbin, M., Sobott, F., White, H.D., Darrow, M., et al. (2020). Need for speed: examining protein behaviour during cryoEM grid preparation at different timescales. *Structure* 28, 1238–1248.
- Levy-Rimler, G., Bell, R.E., Ben-Tal, N., and Azem, A. (2002). Type I chaperonins: not all are created equal. *FEBS Lett.* 529, 1–5.
- Levy-Rimler, G., Viitanen, P., Weiss, C., Sharkia, R., Greenberg, A., Niv, A., Lustig, A., Delarea, Y., and Azem, A. (2001). The effect of nucleotides and mitochondrial chaperonin 10 on the structure and chaperone activity of mitochondrial chaperonin 60. *Eur. J. Biochem.* 268, 3465–3472.
- Magen, D., Georgopoulos, C., Bross, P., Ang, D., Segev, Y., Goldsher, D., Nemirovski, A., Shahar, E., Ravid, S., Luder, A., et al. (2008). Mitochondrial hsp60 chaperonopathy causes an autosomal-recessive neurodegenerative disorder linked to brain hypomyelination and leukodystrophy. *Am. J. Hum. Genet.* 83, 30–42.
- Pockley, A.G., Henderson, B., and Multhoff, G. (2014). Extracellular cell stress proteins as biomarkers of human disease. *Biochem. Soc. Trans.* 42 (6), 1744–1751.
- Polson, E.S., Kuchler, V.B., Abbosh, C., Ross, E.M., Mathew, R.K., Beard, H.A., da Silva, B., Holding, A.N., Ballereau, S., Chuntharpursat-Bon, E., et al. (2018). KHS101 disrupts energy metabolism in human glioblastoma cells and reduces tumor growth in mice. *Sci. Transl. Med.* 10, 454.
- van der Putten, H., and Lotz, G.P. (2013). Opportunities and challenges for molecular chaperone modulation to treat protein-conformational brain diseases. *Neurotherapeutics* 10, 416–428.
- Roh, S.H., Hryc, C.F., Jeong, H.H., Fei, X., Jakana, J., Lorimer, G.H., and Chiu, W. (2017). Subunit conformational variation within individual GroEL oligomers resolved by Cryo-EM. *Proc. Natl. Acad. Sci. USA* 114, 8259–8264.
- Saibil, H.R., Fenton, W.A., Clare, D.K., and Horwich, A.L. (2013). Structure and allostery of the chaperonin GroEL. *J. Mol. Biol.* 425, 1476–1487.
- Satoh, J., Onoue, H., Arima, K., and Yamamura, T. (2005). The 14-3-3 protein forms a molecular complex with heat shock protein Hsp60 and cellular prion protein. *J. Neuropathol. Exp. Neurol.* 64, 858–868.
- Viitanen, P.V., Lorimer, G.H., Seetharam, R., Gupta, R.S., Oppenheim, J., Thomas, J.O., and Cowan, N.J. (1992). Mammalian mitochondrial chaperonin 60 functions as a single toroidal ring. *J. Biol. Chem.* 267, 695–698.
- Viitanen, P.V., Lorimer, G., Bergmeier, W., Weiss, C., Kessel, M., and Goloubinoff, P. (1998). Purification of mammalian mitochondrial chaperonin 60 through in vitro reconstitution of active oligomers. *Meth. Enzymol.* 290, 203–217.
- Weissman, J.S., Hohl, C.M., Kovalenko, O., Kashi, Y., Chen, S., Braig, K., Saibil, H.R., Fenton, W.A., and Horwich, A.L. (1995). Mechanism of GroEL action: productive release of polypeptide from a sequestered position under GroES. *Cell* 83, 577–587.
- Zeng, Y.C., Sobti, M., and Stewart, A.G. (2020). Structural Analysis of a filamentous chaperonin from *Sulfolobus Solfataricus*. *bioRxiv*. <https://doi.org/10.1101/2020.01.13.905216>.

iScience, Volume 24

Supplemental Information

Cryo-EM structure of human mitochondrial HSPD1

David P. Klebl, Matthew C. Feasey, Emma L. Hesketh, Neil A. Ranson, Heiko Wurdak, Frank Sobott, Robin S. Bon, and Stephen P. Muench

Supplementary Figures

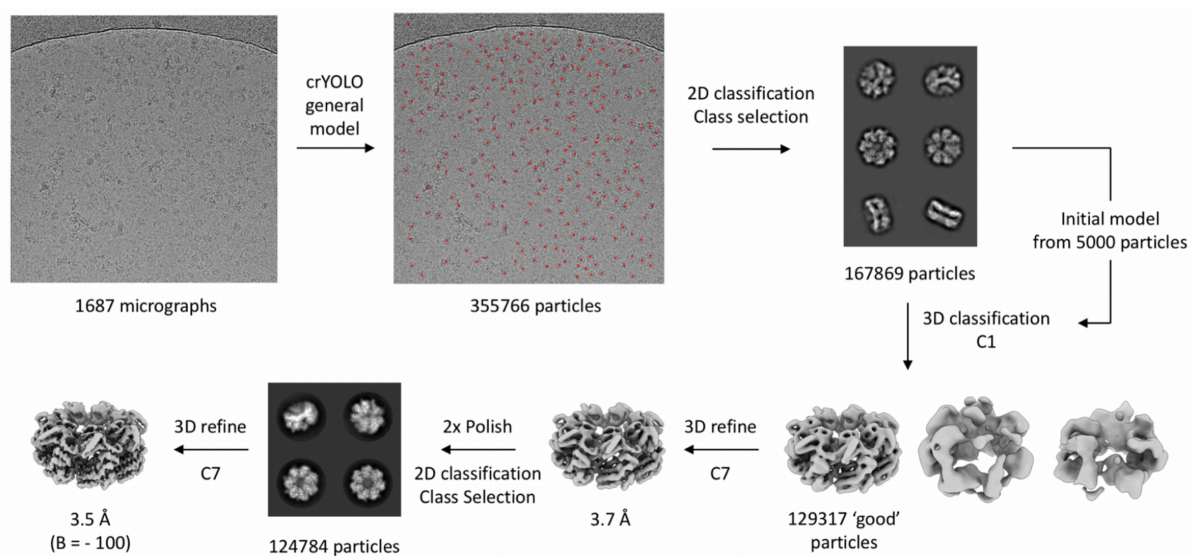


Figure S1. Summary of the data processing pipeline, Related to Table 1. After motion correction and Ctf estimation, particles were picked using the general model in crYOLO. 2D classification yielded 167869 particles, which were subjected to 3D classification. 129317 particles were taken forward to refinement with C7 symmetry and Bayesian polishing. After polishing, 2D classification was used to select the final 124784 particles which were refined with C7 symmetry and filtered by local resolution using a B-factor of -100.

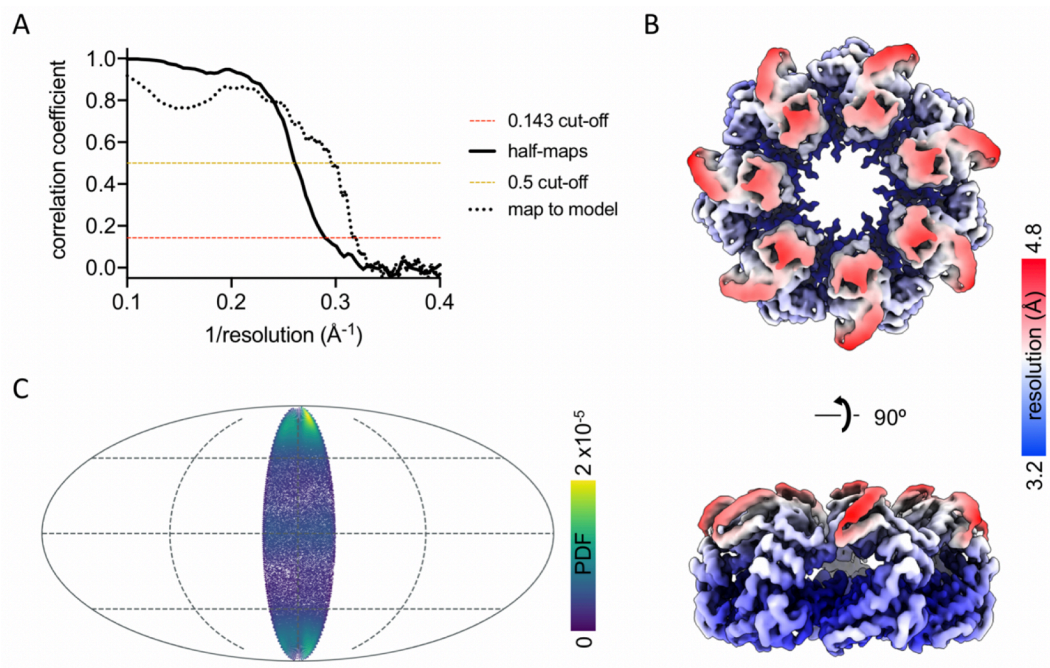


Figure S2. FSC curves, local resolution estimation and orientation distribution for HSPD1, Related to Figure 2. (A) FSC curve for the final HSPD1 single ring reconstruction. Shown are the cut-off at 0.143 (red dashed line), the cut-off at 0.5 (yellow dashed line), correlation

between masked half-maps (black solid line) and correlation between map and model (black dotted line). (B) Local resolution in the HSPD1 single ring reconstruction. (C) Orientation distribution of the HSPD1 single ring particles, shown in Mollweide projection. PDF stands for probability density function, an estimate of the probability of finding a particle in any particular orientation.

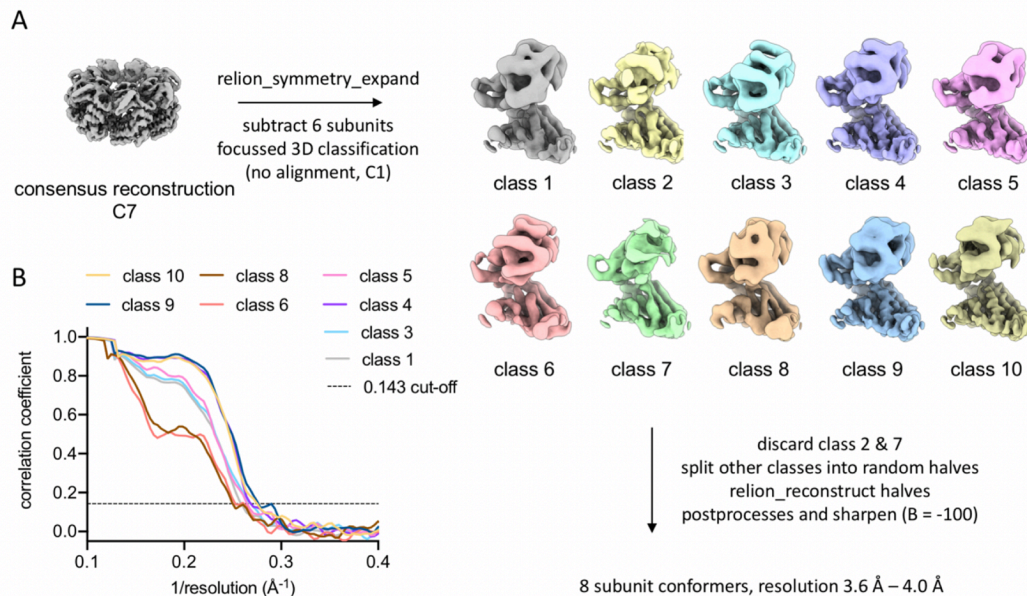


Figure S3. Symmetry expansion of the single ring, Related to Figure 3. (A) Starting point was the consensus reconstruction. The dataset was expanded, 6 of the 7 subunits subtracted and the subtracted particles classified without alignment. Of the 10 classes, 8 were taken forward to reconstruction and postprocessing, resulting in 8 subunit reconstructions at resolutions from 3.6 to 4.0 Å (FSC=0.143). FSC curves for these 8 reconstructions are shown in (B).

Transparent Methods

METHOD DETAILS

Protein expression and purification

An expression plasmid for mature HSPD1 (pMCSG7, containing cDNA for HSPD1, RefSeq NM_002156.4) was kindly provided by Dr Hao Shao and Dr Jason Gestwicki (University of California San Francisco, USA). Expression and purification of HSPD1 were based on a previously described protocol (Viitanen et al., 1998), also described in Klebl et al. 2020. Transformation of competent *E. coli* BL21 DE3 with the plasmid was carried out using the heat shock method (Hanahan 1983). Transformed cells were grown in 20 mL overnight cultures

(TB medium supplemented with 100 µg/mL ampicillin) for ~ 16 h at 37 °C. One litre of TB medium was then inoculated with 10 mL overnight culture and incubated at 37 °C under 200 rpm. When optical density at 600 nm reached 0.8, 250 µM IPTG (final concentration) was added to induce expression of HSPD1. Four hours after induction, the bacterial cells were harvested by centrifugation (10 min, 4000 rpm) and, until further usage, stored at -80 °C.

All purification steps prior to complex reconstitution were done at 4 °C or on ice. All volumes are given per 1 L of culture medium unless stated otherwise. Cell pellets were thawed on ice and resuspended in 20 mL lysis buffer (50 mM Tris, 500 mM NaCl, 10 mM imidazole pH 8), containing 1 mM PMSF and protease inhibitor cocktail (set V, Calbiochem). After further resuspending the cells in a dounce homogeniser, cell lysis was performed using sonication (10 min total, 35% amplitude, 30 sec on/off intervals). The lysate was cleared by centrifugation (30 min, 17,000 rpm) and the supernatant was applied to 3.5 mL Ni-NTA resin (equilibrated in lysis buffer). After washing the resin with 2x 100 mL lysis buffer and 100 mL of 50 mM Tris, 300 mM NaCl, 50 mM imidazole (pH 8), the protein was eluted with 10 mL of 50 mM Tris, 300 mM NaCl, 300 mM imidazole (pH 8). TEV protease (1.6 mg) and DTT (1 mM final concentration) were added and the solution was incubated for 4 h at RT. The cleaved protein was dialysed overnight into 50 mM Tris, 150 mM NaCl pH 7.5 (2 L) using 10 kDa molecular weight cutoff (MWCO) SnakeSkin dialysis tubing (ThermoFisher Scientific). The dialysis product was incubated with 1.5 mL Ni-NTA resin (pre-equilibrated in lysis buffer) for 1 h. The flowthrough was concentrated to 20 – 30 mg/mL in a spin concentrator (Vivaspin, Sartorius, 10 kDa MWCO) after adding 10% (v/v) glycerol. This procedure yielded about 1 - 2 mL at ~ 20 mg/mL per 1 L culture. Four millilitres concentrated, monomeric HSPD1 were mixed with 100 µL KCl (1 M), 100 µL Mg(OAc)₂ (1 M) and 400 µL Mg-ATP (50 mM, pH 7) and incubated for 90 min at 30 °C for reconstitution into oligomers. After centrifugation at 13,000 rpm for 10 min at RT, the supernatant was loaded onto a HiLoad 16/600 Superdex 200 gel filtration column (GE Healthcare) in 50 mM Tris, 300 mM NaCl, 10 mM MgCl₂ (pH 7.7).

Oligomeric and monomeric fractions were collected, pooled and concentrated to 10-25 mg/mL using spin concentrator (Vivaspin, Sartorius, 10 kDa MWCO). Concentrated protein was supplemented with 5% (v/v) glycerol, flash-frozen in liquid N₂ and stored at -80 °C. Protein concentration was measured using absorbance at 280 nm ($\epsilon_{280} = 14,440 \text{ mol}^{-1}\text{cm}^{-1}$, MW = 58.2 kDa). The purity was judged by SDS-PAGE, using Invitrogen™ Bolt™ 4-12% Bis-Tris Plus gels (ThermoFisher Scientific) according to the manufacturer's instructions.

Negative stain EM

For negative stain EM, in-house carbon coated 300 mesh Cu grids were used. Typically, grids were glow discharged in a Pelco easiGlow™ (Ted Pella) at 0.39 mbar, 12 mA for 30 s and used within 30 min. Three microliters of sample were applied to the grid, followed by incubation for 30 s, 2 washes with H₂O and application of 1 % uranyl acetate in two steps (1 min each). Grids were imaged using a FEI Tecnai T12 or a FEI Tecnai F20 microscope. Particle picking and 2D classification were done using crYOLO and RELION 3 (Wagner et al., 2019, Zivanov et al., 2018). Apo HSPD1 was used at 0.02-0.03 mg/mL in gel filtration buffer for negative stain EM.

Native mass spectrometry

For native mass spectrometry, HSPD1 was exchanged into 500 mM ammonium acetate using two consecutive Zeba spin desalting columns (Thermo Scientific) according to the manufacturer's instructions. The protein was diluted to a final concentration of ~ 0.5 mg/mL. Nano-electrospray capillaries were prepared in-house, using a P-97 micropipette puller (Sutter Instrument Co.) and coated with palladium/gold in a Polaron SC7620 sputter coater (Quorum Technologies). Native mass spectra were acquired on an Orbitrap Q Exactive Plus UHMR (Thermo Scientific) operated in positive ion mode. Instrument settings were: 1.5 kV capillary voltage, 20 V in source trapping and HCD off. The AGC target was set to 1e6 with a maximum inject time of 300 ms. The trapping gas pressure (ratio) was 7, resolution 12500 and the mass range was 2000 – 20000 m/z. Spectra were analysed using UniDec (Marty et al., 2015). The experimental error was estimated, for each charge state distribution, by multiplying the half width at half maximum of the most intense peak with the assigned charge.

Cryo-EM grid preparation

For cryo-EM grid preparation, Quantifoil R 1.2/1.3 300 mesh Cu grids were glow-discharged in a Cressington 208 carbon coater (with glow-discharge unit) at 10 mA and 0.1 mbar air pressure for 30 s. Grids were used within 30 min after the glow-discharge treatment. For cryo-EM, oligomeric HSPD1 was used at 2.3 mg/mL in 25 mM Tris, 150 mM NaCl, 5 mM MgCl₂, 1 mM DTT (pH 7.7). Grids were prepared on a Thermo/FEI Vitrobot mark IV, the relative humidity was ≥ 90% and temperature 20 °C. Liquid ethane was used as the cryogen. The blot force was 6 and blot time was 6 s. When grids were prepared with 50 mM Tris, 300 mM NaCl, 10 mM MgCl₂ (pH 7.7) buffer, they contained a small fraction (< 10 %) of inverted double ring particles.

Cryo-EM data collection and processing

Cryo-EM screening and data collection were done using a Thermo/FEI Titan Krios microscope equipped with a Falcon III direct electron detector operated in counting mode at the Astbury BioStructure Laboratory in Leeds. The main data acquisition parameters are given in Table 1 and an overview of the processing strategy is given in Figure S1. All processing was done using RELION 3, unless mentioned otherwise (Zivanov et al., 2018). Briefly, 1687 micrographs were collected. After correcting for beam-induced motion with MotionCor2 (Zheng et al. 2017) and Ctf-estimation using gctf (Zhang 2016), particles were picked using the general model in crYOLO (Wagner et al., 2019). One round of 2 D classification and one round of 3D classification gave a selection of 129317 'good' particles. The resolution (3.7 Å pre-polishing) was improved by 2 rounds of Bayesian polishing and an additional round of 2D classification to 3.5 Å. The final map was obtained by local-resolution filtering in relion using a sharpening B-factor of -100 (Figure S2).

The final particle set was then symmetry-expanded using `relion_symmetry_expand`. Density for six of the seven subunits was subtracted and focussed classification without image alignment was used to split the dataset into 10 classes. Visual inspection of the maps showed clear density for helices H and I in 8 classes, which were taken forward (Figure S3). For each of these classes, particles were split into random halves, each half reconstructed using `relion_reconstruct` and postprocessed (with a sharpening B-factor of -100).

Model building

An atomic model for the HSPD1 single ring was built and refined into the cryo-EM density using Coot, Isolde and Phenix (Emsley et al. 2010, Croll 2018, Liebschner et al. 2019). As starting models, the HSPD1-HSPE1 football crystal structure (PDB: 4pj1) and apo GroEL (PDB: 1xck) were used. Parts of these models were rigid-body docked into the EM density, mutated, and manually adjusted in Coot. The model was then iteratively adjusted and refined in Coot and Phenix. Small adjustments were also made using Isolde. Density was weak or not present for the C-terminus (residues 525-547), probably because these residues are highly flexible. Consequently, they were not modelled. The final model was validated using Molprobit (Chen et al. 2010). Atomic models for reconstructions from symmetry expansion were generated by docking the consensus model into the density and flexible fitting using adaptive distance restraints in Isolde. Atomic models and EM density were visualized using Chimera and ChimeraX (Pettersen et al. 2004, Goddard et al. 2018).

QUANTITATION AND STATISTICAL ANALYSIS

CryoEM data collection and processing were performed as described in single particle data collection and processing sections of the Methods Details using RELION3, MotionCor2, GCTF and crYOLO as detailed in the Key Resources Table.

References:

Chen, Vincent B., et al. "MolProbity: all-atom structure validation for macromolecular crystallography." *Acta Crystallographica Section D: Biological Crystallography* 66.1 (2010): 12-21.

Croll, Tristan Ian. "ISOLDE: a physically realistic environment for model building into low-resolution electron-density maps." *Acta Crystallographica Section D: Structural Biology* 74.6 (2018): 519-530.

Emsley, Paul, et al. "Features and development of Coot." *Acta Crystallographica Section D: Biological Crystallography* 66.4 (2010): 486-501.

Goddard, Thomas D., et al. "UCSF ChimeraX: Meeting modern challenges in visualization and analysis." *Protein Science* 27.1 (2018): 14-25.

Hanahan, Douglas. "Studies on transformation of *Escherichia coli* with plasmids." *Journal of molecular biology* 166.4 (1983): 557-580.

Liebschner, Dorothee, et al. "Macromolecular structure determination using X-rays, neutrons and electrons: recent developments in Phenix." *Acta Crystallographica Section D: Structural Biology* 75.10 (2019): 861-877.

Marty, Michael T., et al. "Bayesian deconvolution of mass and ion mobility spectra: from binary interactions to polydisperse ensembles." *Analytical chemistry* 87.8 (2015): 4370-4376.

Pettersen, Eric F., et al. "UCSF Chimera—a visualization system for exploratory research and analysis." *Journal of computational chemistry* 25.13 (2004): 1605-1612.

Wagner, Thorsten, et al. "SPHIRE-crYOLO is a fast and accurate fully automated particle picker for cryo-EM." *Communications biology* 2.1 (2019): 1-13.

Zhang, Kai. "Gctf: Real-time CTF determination and correction." *Journal of structural biology* 193.1 (2016): 1-12.

Zheng, Shawn Q., et al. "MotionCor2: anisotropic correction of beam-induced motion for improved cryo-electron microscopy." *Nature methods* 14.4 (2017): 331-332.

Zivanov, Jasenko, et al. "New tools for automated high-resolution cryo-EM structure determination in RELION-3." *Elife* 7 (2018): e42166.